SANDIA REPORT
SAND2008-6223
Unlimited Release
Printed September 2008

LDRD Final Report on Bloch Oscillations in Two-Dimensional Nanostructure Arrays for High Frequency Applications

W. Pan, S.K. Lyo, J.L. Reno, J.R. Wendt, and D.L. Barton

Prepared by
Sandia National Laboratories
Albuquerque, New Mexico 87185 and Livermore, California 94550

Sandia is a multiprogram laboratory operated by Sandia Corporation,
a Lockheed Martin Company, for the United States Department of Energy's
National Nuclear Security Administration under Contract DE-AC04-94AL85000.

Issued by Sandia National Laboratories, operated for the United States Department of Energy by Sandia Corporation.

Available to DOE and DOE contractors from
U.S. Department of Energy
Office of Scientific and Technical Information
P.O. Box 62
Oak Ridge, TN 37831

Telephone: (865)576-8401
Facsimile: (865)576-5728
E-Mail: reports@adonis.osti.gov
Online ordering: http://www.osti.gov/bridge

Available to the public from
U.S. Department of Commerce
National Technical Information Service
5285 Port Royal Rd
Springfield, VA 22161

Telephone: (800)553-6847
Facsimile: (703)605-6900
E-Mail: orders@ntis.fedworld.gov
Onlineorder:http://www.ntis.gov/help/ordermethods.asp?loc=7-4-0#online

SAND2008-6223
Unlimited Release
Printed September 2008

LDRD Final Report on Bloch Oscillations in Two-Dimensional Nanostructure Arrays for High Frequency Applications

W. Pan and S.K. Lyo
Semiconductor Materials and Device Sciences Department

J.L. Reno
CINT Science Department

J.R. Wendt
Photonic Microsystems Technologies Department

D.L. Barton
Semiconductor Materials and Device Sciences Department

Sandia National Laboratories
P. O. Box 5800
Albuquerque, NM 87185

Abstract

We have investigated the physics of Bloch oscillations (BO) of electrons, engineered in high mobility quantum wells patterned into lateral periodic arrays of nanostructures, i.e. two-dimensional (2D) quantum dot superlattices (QDSLs).

A BO occurs when an electron moves out of the Brillouin zone (BZ) in response to a DC electric field, passing back into the BZ on the opposite side. This results in quantum oscillations of the electron – i.e., a high frequency AC current in response to a DC voltage. Thus, engineering a BO will yield continuously electrically tunable high-frequency sources (and detectors) for sensor applications, and be a physics tour-de-force. More than a decade ago, Bloch oscillation (BO) was observed in a quantum well superlattice (QWSL) in short-pulse optical experiments. However, its potential as electrically biased high frequency source and detector so far has not been realized. This is partially due to fast damping of BO in QWSLs. In this project, we have investigated the possibility of improving the stability of BO by fabricating lateral superlattices of periodic

coupled nanostructures, such as metal grid, quantum (anti)dots arrays, in high quality GaAs/Al_xGa_{1-x}As heterostructures. In these nanostructures, the lateral quantum confinement has been shown theoretically to suppress the optical-phonon scattering, believed to be the main mechanism for fast damping of BO in QWSLs. Over the last three years, we have made great progress toward demonstrating Bloch oscillations in QDSLs. In the first two years of this project, we studied the negative differential conductance and the Bloch radiation induced edge-magnetoplasmon resonance. Recently, in collaboration with Prof. Kono's group at Rice University, we investigated the time-domain THz magneto-spectroscopy measurements in QDSLs and two-dimensional electron systems. A surprising DC electrical field induced THz phase flip was observed. More measurements are planned to investigate this phenomenon. In addition to their potential device applications, periodic arrays of nanostructures have also exhibited interesting quantum phenomena, such as a possible transition from a quantum Hall ferromagnetic state to a quantum Hall spin glass state.

It is our belief that this project has generated and will continue to make important impacts in basic science as well as in novel solid-state, high frequency electronic device applications.

Table of Contents

Accomplishments

We have made great progress toward demonstrating Bloch oscillations in two-dimensional (2D) nanostructure arrays, e.g., metal grids and quantum (anti)dot superlattices (QDSL). We have observed a negative differential conductance and the Bloch radiation induced edge-magnetoplasmon resonance. In collaborating with Prof. Kono's group at Rice University, we have also performed the time-domain THz magneto-spectroscopy measurements in QDSLs and in two-dimensional electron systems. During the past three years, numerous invited and contributed presentations were given, and four papers were published and submitted by team members. Overall, this project has generated and will continue to make important impacts in basic science as well as in novel solid-state, high frequency electronic device applications.

In the following, we list a few results that manifest our progress. Firstly; a negative differential conductance (NDC) was seen at high source-drain bias (V_{dc}) in the I-V measurements. It is known that the occurrence of a BO and the associated Bragg-diffraction can induce a NDC. Our observation of this NDC may represent the first evidence of Bloch oscillations in 2D QDSLs. Secondly; in our magneto-transport experiments, under high V_{dc}, a resonance-like resistance spike was observed. The value of the magnetic (B) field where the spike occurs varies as V_{dc} is changed. In fact, when plotting V_{dc} vs B, a relationship of $V_{dc} \propto 1/B$ is observed. This 1/B dependence is probably due to the so-called edge-magnetoplasmon resonance (EMP). EMP resonance has been observed before in quantum dot array samples, however, under external high frequency radiation. In comparing with previous experiments, we can conclude that in our QDSL experiment the required high frequency radiation is probably provided by electron self-radiation, i.e., BO. Thirdly; in the time-domain THz magneto-spectroscopy measurements, a surprising DC electrical field induced THz phase flip was observed. FFT analyses seem to show possible evidence of THz gain due to Bloch oscillations in QDSLs. Fourthly; we studied the quantum physics under extreme conditions in QDSLs. At very low temperatures and high magnetic fields, fully developed quantum Hall states are observed at the Landau level fillings nu = 1, 2… What's really interesting is that the strength of the nu = 1 state is significantly reduced. This observation is a totally surprise and vastly different from a bulk and unpatterned sample where the nu = 1 quantum Hall state is very strong. We believe that this weakening of the nu = 1 state and collapse of its energy gap at a critical effective disorder is due to a possible transition from a quantum Hall ferromagnetic state to a quantum Hall spin glass state. Finally; samples with different pitches and depths have been fabricated using the state-of-the-art E-beam lithography and interferometric lithography techniques.

These above results are important for an ultimate direct demonstration of BO in QDSLs, and extremely well suited to Sandia's unique expertise in RF electronics and quantum nanoelectronics.

Introduction

Bloch oscillation

Bloch oscillation (BO) [1] was originally proposed for electrons in three-dimensional (3D) crystals. Under an external electric field E, if an electron reaches the boundary of Brillouin zone (BZ) without being scattered, it undergoes Bragg reflection, passing back into the BZ on the opposite side. This results in a high frequency (f) quantum oscillation of electron at f = eEd/h, where d is the period of potential and h is Planck constant. However, natural mechanisms in 3D [2], such as electron scattering and Zener tunneling, occur before the electrons can complete a full oscillation, preventing the realization of BO. Realizing this difficulty, Esaki and Tsu [3] proposed using vertical quantum well superlattices (QWSLs). As shown in Fig.1, in this structure, the finite tunneling between two quantum wells creates so-called mini conduction bands and, thus, easily traversed mini-BZ's. While tantalizing indirect evidence of BO's has been obtained in QWSL with complex optical techniques [4], to date no direct evidence in electrical transport has been observed.

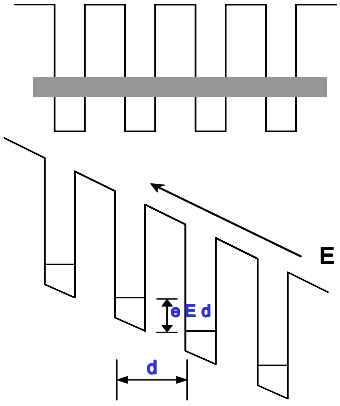

Fig. 1 Schematic conduction-band diagram of quantum well/dot superlattice of period d, without (top) and with (bottom) electrical field E. Wannier-Stark ladder is shown in the bottom plot. When an electron jumps from one ladder to the immediate lower ladder, a photon is emitted. This is Bloch oscillation. The frequency of Bloch oscillation is f = eEd/h.

The primary difficulties preventing Bo in the QWSL approach are (1) fast damping of oscillations by electron-optical phonon scattering, and (2) electric field domain formation [5], which is intrinsically related to the existence of the Wannier-Stark ladders and the so-induced negative differential conductance, and is believed to be even more detrimental in destroying BO. In the past, several ideas have been proposed to circumvent this problem, for instance, to replace the DC field with a strong AC field of a driving frequency much faster than the domain formation rate. However, this implies a need for cumbersome high frequency equipments. Another possibility to stabilize the electrical field in a QWSL is to shunt the current flow by semiconductor material at the superlattice edges [6]. But, fabricating this device structure is a daunting technical challenge.

To overcome these technical obstacles, we propose to generate BO in lateral superlattices of periodic coupled nanostructures, *i.e.*, quantum dot superlattices (QDSLs). A quantum dot is a semiconductor analog of an "atom". Inside of a quantum dot, the motion of an electron is confined in all three dimensions by an engineered potential well and its energy is quantized into a series of eigenstates. This complete quantization is very similar to an electron in an atom. When many quantum dots form a periodic crystal lattice, or QDSL, the coupling between dots leads to the formation of coherent bonding-antibonding states, and thus the so-called Bloch minibands. When biased with an external electric field, a

miniband transforms into even-spaced Wannier-Stark ladders (as shown in Fig.1), and BO is generated. Depending on the magnitude of DC electric field (*e.g.*, ~ 10kV/cm) and the period of superlattice (50-350nm), the BO frequency can be continuously tuned from ~70GHz (in the region of millimeter wave) to ~500GHz (the lower end of terahertz regime). In contrast to QWSL, in QDSL, by varying the strength of electric field and its orientation with respect to the crystal axes, it is possible to suppress completely the electron-optical phonon scattering [7]. As a result, the BO damping time, even at room temperature, may exceed the BO period. Furthermore, in QDSL, varying the coupling strength between two quantum dots allows us to finely tune the junction resistance. A finite junction resistance can be used as the shunt resistance, and may help to stabilize the electrical field in QDSL and prevent formation of electric field domains.

Shallow two-dimensional electron systems

This project proposes to fabricate novel periodic coupled nanostructures, i.e. a quantum dot superlattice, for generating coherent Bloch oscillation, and to use it as new source and detector for high frequency electromagnetic radiation. One of the challenges we had to face is the firm control of the quantum dot size. This will determine the overlap between two quantum dots. For this purpose, a shallow (*e.g.*, ~ 80 nm below sample surface) yet high mobility two-dimensional electron gas (2DEG) is desired. These two requirements generally are traded against one another, but we have led the efforts to achieve this ability. Recently, we have shown that for a 2DEG about 80nm below surface electron mobility higher than $\mu=1x10^6$ cm^2/Vs can be achieved (after illumination with a LED at low temperatures), as shown in Figure 2.

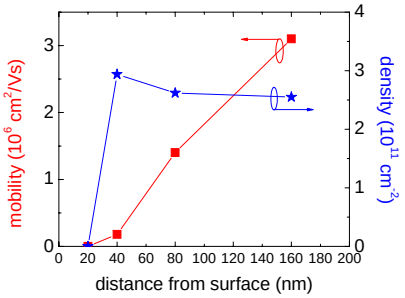

Fig.2 Electron density and mobility versus the distance between 2DEG and surface.

Nanostructures patterning

QDSLs are created by E-Beam lithography [8] and interferometric lithography [9] techniques. The high-resolution electron-beam lithographic techniques are best adapted to create arbitrarily shaped and positioned nanoscale features. The flexibility of electron-beam lithography, combined with controlled chemical wet etching, allows us to fabricate QDSLs with different geometry, *i.e.*, square, rectangular, triangular, honeycomb lattices. This rich choice of the symmetry of electron confinement provides access to a large parameter space to optimize QDSL for the eventual observation of Bloch oscillation.

Here, we show some impressive results, taken by Joel Wendt, from an initial exposure of a relatively new positive e-beam resist, ZEP520A, on the JEOL 9300FS, the newly equipped E-Beam machine at Sandia. A primary benefit of this resist is its superior etch resistance as compared to PMMA, but it also has excellent resolution and good process latitude. The resist thickness is a ‘standard’ and practical 300 nm, relatively thick for the

sub-100 nm features being exposed. Figure 3a shows two 10 μm squares exposed with a 0.1 μm gap between them and the resulting 0.1 μm line left behind. Normal PMMA just wouldn't be able to achieve this, as the line would blow out in the middle without some fancy proximity correction. Figs. 3b and 3c show 1-D and 2-D gratings at 100 nm pitch with features down to 25 nm with excellent uniformity. These features were evident across a relatively wide dose range (200-240 μC/cm2).

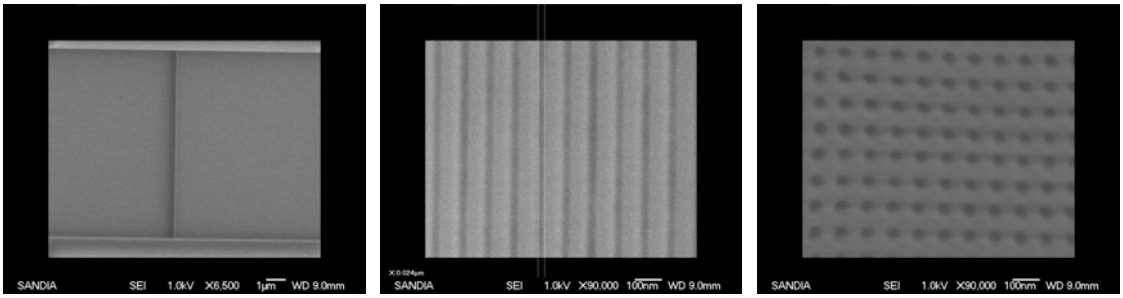

Fig. 3a Fig. 3b Fig. 3c

Fig. 3: E-beam patterns using a new positive e-beam resist.

The interferometric lithography (IL) is a perfect tool to create a macroscopic array, with overall dimensions extending from mm to cm of nanometer scale features. We have established a fruitful collaboration with Professor Steve Brueck at the University of New Mexico for using state-of-the-art IL technique to fabricate QDSLs.

Negative differential conductance in two-dimensional electron grids

Introduction

In a periodic structure of electron potential, under an external electric field *E*, if an electron can reach the boundary of the Brillouin zone (BZ) without being scattered, it undergoes Bragg reflection, passing back into the BZ on the opposite side. This results in a high frequency (*f*) quantum oscillation of electron, i.e., Bloch oscillation (BO), at $f = eEd/h$, where *d* is the period of the potential, *e* is the electron charge, and *h* is Plank's constant. When the magnitude of electric field and the period of potential are properly chose, the Bloch frequency can fall in the terahertz (THz) region. Proposed about 80 years ago [1], recently, BO has gained a renewed interest, as a Bloch oscillator can be utilized as a solid-state, electrically-biased, frequency-tunable THz source and detector.

So far, work on BO has mainly been carried out in vertical quantum well superlattice structures [3, 10-17]. On the other hand, a surface superlattice patterned in a two dimensional electron system (2DES) has long been proposed as an alternative device structure to generate BO [18-23]. A surface superlattice has three-dimensional quantization, as opposite to the conventional vertical quantum well superlattice [20]. As a result, gaps in the energy spectrum exist in all three dimensions. This provides the possible existence of BO at relatively moderate electric field. It has also been shown that

[20, 23], in surface superlattices, the electron-optical phonon scattering, one of the limiting mechanisms in achieving BO in the THz range in vertical superlattice, can be completely suppressed, and electrically generated BO can become possible. Furthermore, compared to a vertical superlattice, a surface superlattice offers various other advantages, for example, easy device fabrication and multiple fundamental frequencies. It can also fully utilize the benefit of long coherent transport time achieved in high mobility 2DES. To date, however, very few studies of BO in surface superlattices have been reported.

Here, we report the experimental observation of negative differential conductance in surface superlattices, one of the signatures of BO. Two devices with varying coupling strengths are studied and in both samples NDC is observed. Our theoretical simulation, based on an energy relaxation-time approximation and a microscopic short-range elastic scattering model for the momentum relaxation [24], yields reasonable agreement with the experiment data.

Device fabrications

To minimize electron scattering by residual impurities and to achieve long coherent transport time, the starting material is a high mobility 2DES realized in a GaAs quantum well (QW) of width 300Å. The low temperature density and mobility of 2DES are n ~ 2-3x10^{11} cm^{-2} and $\mu > 1x10^6$ cm^2/Vs, respectively, before patterning. After the patterning, the electron mobility was reduced somewhat. Two specimens (sample A and sample B), cut from two wafers, were studied. The growth structure for the two wafers basically is the same, except that in wafer A the quantum well is 200 nm below the surface, while in wafer B 150 nm below. A low frequency lock-in technique was used to measure the low-temperature magnetoresistance (R_{xx}) and a Keithley K236 source meter was used to supply the source-drain DC bias (V_{dc}) and to measure the source-drain current (I_{ds}).

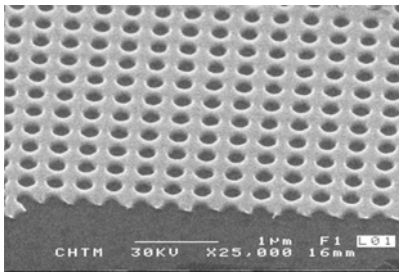

Fig. 4 SEM picture of a metal grid device.

In our experiments, a surface superlattice was realized in a two-dimensional (2D) electron grid device. The 2D electron grid was fabricated by depositing a periodic 2D metal grid on the surface of QW samples. The metal consists of Ti/Au, about 80 nm thick. A SEM picture of metal grid is shown in Fig. 4. The pitch of the metal grid is ~ 350 nm and diameter of the holes ~ 150 nm. To achieve this large-area nanometer scale patterning, the interferometric lithography technique was employed [25]. In experiments, the grid devices were cooled in darkness to 4K and a low temperature illumination by a red-light-emitting-diode was used to realize the low temperature density and mobility. During each cool down, the sample, including the metal grid was grounded. Due to the different thermal expansion coefficients of the metal and the GaAs/AlGaAs

semiconductor, the mechanical stress induces a two-dimensional electron potential modulation of the 2DES.

Results and discussions

To characterize this modulation, we have adopted well-documented methods [26] by measuring R_{xx}, as shown in Figure 5. Similar to previous results, a positive magnetoresistance near zero magnetic (*B*) field and the commensurate oscillations (marked by the red triangles) were observed. From the saturation *B* field of the positive magnetoresistance [27], we estimated that the modulation amplitude is ~ 3% of the Fermi energy (E_F) (or ~ 0.3 meV) for sample A, and 15% (~ 1 meV) for sample B. To compare, in a reference sample without patterning neither positive magnetoresistance nor commensurate oscillation was observed in R_{xx}.

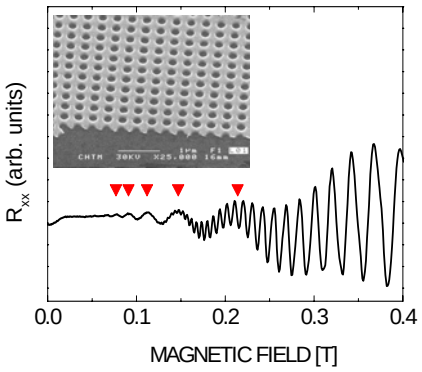

Fig.5 Magnetoresistance of a QDSL. The low field, low frequency oscillations are due to commensurate resonance, confirming the feasibility of electronic potential modulation by the QDSL. The high field ones are the Shubnikov-de Haas oscillations. The inset shows the QDSL pattern.

Current-voltage (I-V) measurement was carried out at 4K, using a Keithley K236 source meter. In Fig.6, the I-V curves of sample A and sample B are shown. At small V_{dc}, both devices show ohmic behavior, and the corresponding resistance is ~ 1500 Ω for sample A and ~3000 Ω for sample B. These resistances include wire and contact resistance in addition to the sample resistance. In sample A (Fig. 6a), I_{ds} reaches a maximal value of ~ 0.92 mA at V_{dc} ~ 2.7 V, and then decreases as V_{dc} continues to increases, reaching a local minimum of 0.89 mA around ~ 6.5V. After this, I_{ds} increases again with increasing V_{dc}. In other words, a negative differential conductance is observed between ~ 2.7V and ~ 6.5 V. In sample B where a stronger modulation is achieved, again, a NDC is observed. In Fig. 6b and Fig. 6c, we show the I-V curves from two different cool-downs. Two features are worthwhile emphasizing: 1) The maximal current is significantly higher than that in sample A, ~ 2.5 mA at V_{dc} ~ 3.8 V; 2) More complex structures are observed in the NDC regime. In particular, in Fig. 6c, 3 current jumps are observed at V_{dc} ~ 3.8, 4.0, 4.6 V.

The observation of NDC is exciting. Recall that NDC was predicted and taken as the evidence of Bloch oscillations in vertical quantum well superlattices by Esaki and Tsu in their original paper [2]. In surface superlattices, it was shown [18-23] that the bend-over in the I-V curve could also be due to the onset of Bloch oscillations, where electrons are able to cycle many times through the reduced Brillouin zone before a scattering even can happen [20]. Thus, the observed NDC may indeed represent the evidence of electron self-oscillations in our 2D electron grids. Furthermore, the I-V curves show different characteristics in the two samples, indicating that the I-V characteristics and the 2D electronic transport properties can be manipulated by adjusting the structure. Finally, we note the observation of current jumps in the NDC region in our GaAs surface superlattice. Similar current jumps have been observed in InGaAs/InAlAs vertical superlattices [28]

and in InAs/AlSb resonant-tunneling diodes [29], and were attributed to self-rectification of the electron oscillation [30].

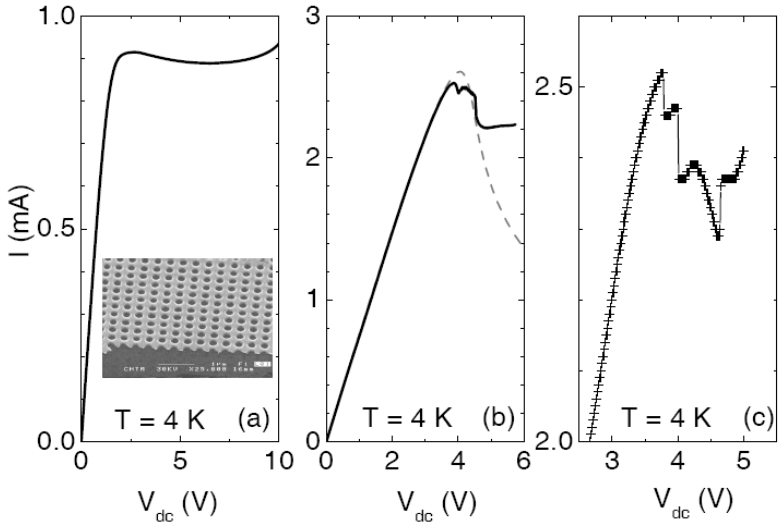

Fig. 6 (a) I-V trace in sample A. (b) I-V trace in sample B. Gray dash line represents the theoretical data. (c) Zoom-in plot of I-V trace in a different cool-down for sample B. Jumps in current in the negative differential conductance regime are apparent.

Of course, other mechanisms, such as the formation of high electric-field domains and the so-called thermal runaway, can also induce an apparent NDC. It has been shown that stationary or propagating domains can form in 2D structures [31]. In this regard, it is possible that current jumps might be produced as the domain boundary moves through the interface fluctuations induced by surface superlattice [32]. On the other hand, the two-dimensional nature of conducting channels may help to stabilize the electrical field in surface superlattices and prevent the formation of high electric-field domains. It is interesting to study in future experiments whether the current jump observed in our device is related to the domain formation.

To experimentally eliminate the possibility of thermal runaway origin, we employ a "differential" measurement setup (as shown in the inset of Fig. 7), where a thin film resistor of constant value R_0 = 1500 Ω is connected in series with the two-dimensional electron grid (sample B). A small alternating current bias (V_{ac}) is added to V_{dc}. The voltage measured by a lock-in amplifier is given by $V = V_{ac} \times R_0/(R_0+r)$, where $r = dV/dI$ is the differential resistance of the two-dimensional electron grid. Here, we have omitted the wire and contact resistance, since they are relatively small compared to $|r|$ in the NDC region. If the observed NDC is of thermal runaway origin, r is always positive. Consequently, V is expected to be positive, at any V_{dc}. On the other hand, if r is caused by dynamic localization through BO, then $r < 0$. In the case of $|r| >> R_0$, V is expected to be negative in the NDC region. In Fig.8, we show V as a function of V_{dc}. At small V_{dc}, V is nearly constant, consistent with the observation in Fig. 1 that our electron grid is ohmic at small V_{dc}. Starting from $V_{dc} \sim 8$V, V begins to decrease. At $V_{dc} \sim 8.9$V, V becomes negative [33]. The observation of negative V shows that, indeed, the observed NDC is not a result of thermal effects.

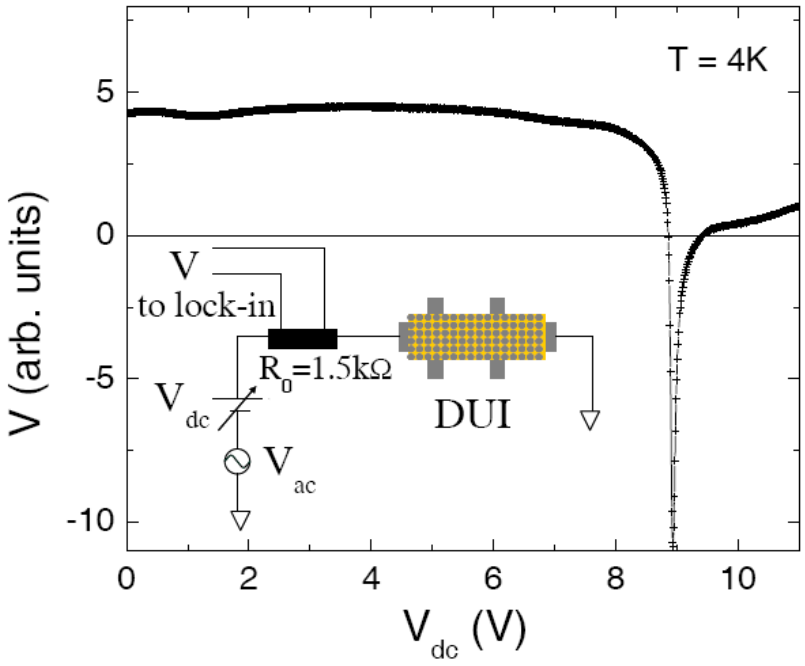

Fig. 7 "Differential" measurement for verifying the thermal runaway origin of the observed NDC. The inset shows the experimental setup. R_0 is a thin-film resistor.

To help understand the physical origin of NDC, a theoretical study was carried out for sample B with 15% modulation. We first calculate the energy band structures. In our device with a periodic in-plane potential modulation, the original modulation-free single conduction band is folded into many Bloch mini-bands with small mini-band gaps. Surprisingly, each mini-band can be represented by a few-component cosine function (similar to Esaki's band) with negligible contributions from higher harmonics. To calculate the I-V characteristic, we use a model similar to that by Gerhardt [24], except that our model treats a degenerate two-dimensional (2D) electron gas and assumes that the matrix element for elastic scattering is independent of the initial and final momentum (relevant to short-range impurity potentials), thereby treating 2D interband scattering with an equal weight. Also, in our calculation, a simplified model, where the electron potential modulation is one-dimensional in the field direction, is used. We believe that the physics for a qualitative understanding should essentially be the same as in the two-dimensional electron grid. Details of our theoretical calculations will be published elsewhere. The theoretical result is shown in Fig. 7b by the gray dash-line. Overall, the theoretical result is in a reasonable agreement with the experimental data, except that the decrease of current in the NDC regime is steeper than that of the experimental data. We also note here that the effective current cross section employed in theoretical calculations is smaller than the geometric cross section of real device by a factor of a few, and the electron scattering rate is larger than that deduced from the mobility. Those discrepancies probably are related to the assumptions of 1) a 1D model and 2) field-independent inelastic scattering rate we made in the calculation. Finally, for a self-consistent check, for a parabolic band in the absence of periodic potential modulation, our model yields linear field dependence of current and therefore no NDC.

Summary

In conclusion, we have observed a negative differential conductance (NDC) in two-dimensional electron grid devices, and in one sample, several current jumps in the NDC region. Our theoretical modeling yields reasonable agreement with the experimental data. The observed NDC might represent the evidence of Bloch oscillation in our two-dimensional electron grids.

Bloch oscillations induced edge magnetoplasmon resonance

Introduction

A two-dimensional electron system under periodic electronic potential modulation (i.e., QDSLs) and in quantizing magnetic field has been a model system to study electron dynamics. Over the years, many interesting phenomena have been discovered, for example, the edge magnetoplasmon resonance and the evidence of Butterfly spectrum.

In a series of theoretical papers by Dmitriev and Suris [7], this structure of periodic arrays of weakly coupled quantum dots were thoroughly studied. In QDSL, the coupling between dots leads to the formation of coherent bonding-antibonding states, and thus the minibands. When biased with an external electric field, BO is expected to be generated. In contrast to QWSL, Dmitriev and Suris [7] showed that in QDSL, by varying the strength of electric field and its orientation with respect to the crystal axes, it is possible to suppress completely the electron – optical phonon scattering. Consequently, the BO damping time, even at room temperature, may exceed the BO period by several hundred times, therefore, making the observation of BO possible in electronic transport measurements.

Experimental results and discussions

In this section, we show results obtained from a metal grid sample, one type of QDSLs. Metal grid is created by inteferometric lithography technique combined with the lift-off technique.

We have performed magnetotransport studies in this metal grid sample, and observed very exciting results. These results, we believe, may provide the first experimental evidence of Bloch oscillation (BO) in two-dimensional superlattice systems. In the experiment, we used four-terminal measurement technique. A fixed DC bias (V_{dc}) was applied between the source and drain, and the voltage drop across a pair of voltage leads was measured by a HP digital multimeter. At the same time, the magnetic (B) field was swept from 0 to 1T. In Fig. 8a, we show a single trace at V_{dc} = 1.4T. It is clearly seen that in whole B field range, V_{xx} varies quite smoothly, except at B ~ 0.35T where a resonance-like resistance spike is observed. In Fig. 8b, we show a series of traces at various V_{dc}'s. Interestingly, the spike only occurs at high V_{dc} and disappears when V_{dc} is small. For example, at V_{dc} = 1.2V, no spike is apparent. In Fig.8c, we plot V_{dc} as a function of the B field where the spike occurs. Overall, it shows a dependence of $V_{xx} \propto 1/B$.

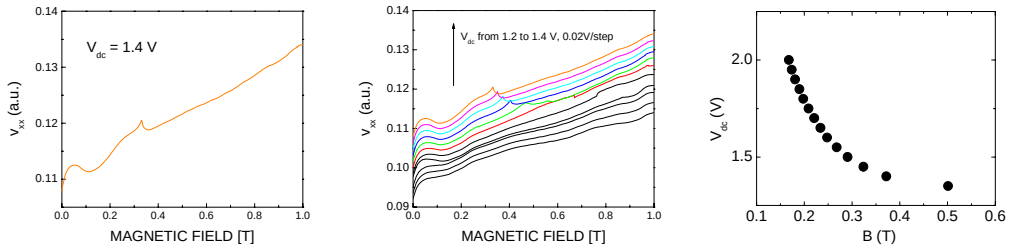

Fig.8 a) Voltage drop across a pair of leads V_{xx} vs B at a source and drain bias V_{dc} = 1.4 V. A resonance-like spike is clearly seen at B ~ 0.35 T. b) V_{xx} vs B at several V_{dc}'s. c) V_{dc} as a function of the B field where the spike occurs. This set of data was obtained from the same sample, however, in a different cool-down.

This 1/B dependence is exciting. To understand the physical origin of this 1/B dependence, we first point out that a similar 1/B dependence has been observed long before in a two dimensional semiconductor disk array under high frequency microwave radiation. It has been explained to be due to the so-called edge magnetoplasmon resonance [34], and its dispersion relationship is given by the following formula

$$\omega = -\omega_c/2 + (\omega_0^2+(\omega_c/2)^2)^{1/2},$$

where ω is the resonance frequency, ω_c is the cyclotron resonance frequency, and ω_0 is the plasmon frequency, determined by sample size. At high B fields where $\omega_c >> \omega_0$, $\omega \propto$ 1/B. Considering the similarity between our result and previous ones, we think that the 1/B dependence in the metal grid might also be due to the edge magnetoplasmon resonance. Compared to previous experiments, however, no external radiation was applied to our metal grid. The required high frequency radiation, we believe, is due to the self-oscillation of electrons, i.e., Bloch oscillation. In other words, under a large V_{dc}, Wannier-Stark ladders are formed, and BO is generated. This high frequency radiation is then self-absorbed by the 2D electron system itself, coupled to the plasmon and cyclotron motions, which gives rise to the edge-magnetoplasmon resonance.

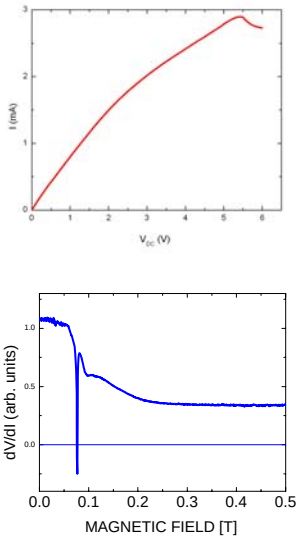

Fig.9 Top panel shows the I-V characteristic in a 2D anti-dot array device. Bottom panel shows the resonant behavior in magneto-transport in the same device.

The above traces were obtained in a metal grid sample. To address the effect of the metal grid on the surface of the quantum dot superlattice (QDSL) devices, we fabricated the two-dimensional "anti-dot" arrays without metal gird. In this new device, wet etching technique was utilized to "drill" holes on the top of the sample surface and thus to induce electrical potential modulation. Again, the negative differential conductance and the resonance-like magneto-transport

behavior were observed, as shown in Fig. 9.

Before we finish this section, a few of remarks are inline. First, it is surprising that a collective, resonance-like can be generated, especially with so many electrons in our system. In previous work on Bloch oscillations in 1D QWSLs, the structures were not doped and a short laser pulse was used to generate a coherent electron ensemble. In our specimen, however, the carriers' density is high, about $2x10^{11}$ cm^{-2}. Their motion is most likely incoherent. Perhaps, by adding a magnetic field and forcing the electrons to undergo plasmon oscillations, it now becomes possible to generate a phase coherent ensemble of 2D electrons.

Second, we notice that the resonance like behavior in the specimen with a metallic grid on the surface is much stronger than that in the specimen without a metallic surface. This might be due to the fact that the coupling between the BO induced radiation and the 2DES becomes more efficient, through reflection of the metallic grid.

Finally, the weak resonant behavior at high bias might be a temperature effect. In our experiment, the refrigerator temperature was kept at 4K. At small Vdc, e.g., Vdc = 1.4 V, the temperature reading from a nearby thermometer showed that the experimental temperature was still close to 4K. However, we did observe a heating effect at high DC biases.

Summary

To summarize, we have observed in later quantum dot arrays (or quantum dot superlattice) the negative differential conductance and a resonance –like behavior in the magnetic field. We show that this resonance like behavior is probably due to Bloch oscillations induced edge magnetoplasmon resonance.

Theoretical studies of Bloch oscillations in lateral 1D superlattices

Introduction

Electrons driven by a high electric field E sweep through a Bloch band and yield oscillations in k space as well as in the real space. The oscillations are damped before the electrons sweep through the band many times because of scattering, reaching a steady state and yielding the negative differential conductance. This fascinating phenomenon has received much attention in the past for its potential to yield THz generation and also for applications to negative differential conductance [3,13,24,35-45]. Esaki and Tsu [3] predicted that negative differential conductance can be observed in semiconductor superlattices without applying a huge electric field due to their large lattice periods, small Brilloin zones, and narrow bandwidths. Investigations of Bloch oscillations have been carried out in THz emission [46-49], electro-optic detection [49,50], and four-wave mixing experiment [51].

In an extremely high field where the potential energy drop between the superlattice cells is larger than the bandwidth, full quantum mechanical approach in terms of Wannier-Stark ladders is convenient and conduction occurs through phonon-assisted hopping down the Stark Ladder [43,52]. In the opposite (but still nonlinear) limit, however, a semiclassical formalism based on the Boltzmann equation is preferable in studying the scattering effect. It is difficult to consider the interband tunneling effect in this approach. This effect is negligible if the bandgap is very large. In this paper, we present an exact analytic result for the time-dependent current and the distribution function in the latter nonlinear limit for a degenerate and non-degenerate electron gas in a one-dimensional superlattice miniband by employing a relaxation-time approximation for inelastic scattering with a constant (i.e., energy-independent) relaxation rate. The current model is relevant to a quantum wire with a periodically modulated potential. The final transparent analytic results show clearly the distinct roles played by elastic and inelastic scattering in competition with the driving force for the damped Bloch oscillations and the steady-state current. They also show quantitatively how scattering damps the Bloch oscillation, the condition for the onset of the oscillations, and also the oscillation frequency. The present approach can serve as a guide to understanding the results of a more complicated full numerical treatment. A recent full numerical study which replaces the present relaxation-time approximation of inelastic scattering by microscopic electron-phonon scattering processes yielded results very similar to those predicted here [53]. A similar relaxation-time approach based on an iterative numerical solution [24] was employed earlier for a three-dimensional system for the steady-state current and yielded results qualitatively similar to those based on a microscopic treatment [40].

Relaxation-Time Model

While our model can be generalized to multibands, we will study only the single-band situation for clarity. The time-dependent rate equation for the distribution function f(k,t) is given by

$$\frac{\partial f(k,t)}{\partial t} - \frac{eE}{\hbar}\frac{\partial f(k,t)}{\partial k} = -\nu_{\text{in}}[f(k,t) - f^{(0)}(\varepsilon_k)] - \nu_{\text{el}}(k)[f(k,t) - f(-k,t)], \quad (1)$$

where ν_{in} is a phenomenological inelastic scattering rate assumed to be a constant [24], $f^0(\varepsilon,k)$ is the Fermi function, and $\nu_{el}(k)$ is the elastic scattering rate given by

$$\nu_{\text{el}}(k) \equiv \frac{\pi}{2\hbar}|U(2k)|^2 D(\varepsilon_k). \quad (2)$$

Here, U(2k), D(ε_k})$ are the matrix element for the back scattering and the density of states at the energy ε_k, respectively. The total particle number is conserved in Eq.1 at all times. Here, we obtain the steady-state current for an arbitrary scattering potential U(2k) and the time-dependent current as well as the distribution function for a constant ν_{el}. In

the present one-dimensional lattice, the expression for elastic scattering in Eq.1 is exact in contrast to the past studies in three dimensions. In the latter case, similar back-scattering model ν_{el} [f(**k**,t) - f(-**k**,t)] was employed by Ktitorov el al. [35] for a constant ν_{el}, neglecting elastic scattering to other directions. Similarly, Ignatov et al [41] studied the elastic momentum-relaxation model ν_{el} [f(k_z,t) - f(-k_z,t)], where k_z is the crystal momentum in the direction of the electric field.

Defining

$$F^{\pm}(x,t) = [f(k,t) \pm f(-k,t)]/2, \tag{3}$$

from Eq.1 we obtain

$$\frac{\partial F^{+}(x,t)}{\partial t} - \frac{\partial F^{-}(x,t)}{\partial x} = -\nu_{\text{in}}[F^{+}(x,t) - f^{(0)}(\varepsilon_k)], \tag{4}$$

and

$$\frac{\partial F^{-}(x,t)}{\partial t} - \omega_E \frac{\partial F^{+}(x,t)}{\partial x} = -\tilde{\nu}(k) F^{-}(x,t), \tag{5}$$

where ω_E= eEa/ , x = ka, a is the superlattice period, and

$$\tilde{\nu}(k) = \nu_{\text{in}} + 2\nu_{\text{el}}(k). \tag{6}$$

We now carry out the Laplace transformation for the above expressions employing the notation

$$\mathcal{F}^{\pm}(x,s) = \int_0^{\infty} F^{\pm}(x,t) e^{-\text{st}} dt. \tag{7}$$

using the initial conditions $F^{-}(x,0) = 0$, $F^{+}(x,0) = f^{0}(\varepsilon_k)$, and find

$$\omega_E \frac{\partial \mathcal{F}^{-}(x,s)}{\partial x} = (\nu_{\text{in}} + s)\mathcal{F}^{+}(x,s) - \left(1 + \frac{\nu_{\text{in}}}{s}\right) f^{(0)}(\varepsilon_k), \tag{8}$$

and

$$\omega_E \frac{\partial \mathcal{F}^{+}(x,s)}{\partial x} = [\tilde{\nu}(k) + s]\mathcal{F}^{-}(x,s). \tag{9}$$

We then find from Eqs.8 and 9

$$\frac{\partial^2 \mathcal{F}^{-}(x,s)}{\partial x^2} = A(x)\mathcal{F}^{-}(x,s) - C\frac{\partial f^{(0)}[\varepsilon(x)]}{\partial x}, \tag{10}$$

where

$$A(x) = (\nu_{\text{in}} + s)[\tilde{\nu}(k) + s]/\omega_E^2, \quad C = \left(1 + \frac{\nu_{\text{in}}}{s}\right)/\omega_E. \quad (11)$$

Equation 10 is solved by expanding

$$\mathcal{F}^-(x,s) = \sum_{m=1}^{\infty} \mathcal{F}_m^-(s)\sin(mx),$$

$$\mathcal{F}_m^-(s) = \frac{2}{\pi}\int_0^{\pi} \mathcal{F}^-(x,s)\sin(mx)dx, \quad (12)$$

$$A(x) = \sum_{m=0}^{\infty} A_m \cos(mx),$$

$$A_m = \frac{2}{\pi(1+\delta_{m,0})}\int_0^{\pi} A(x)\cos(mx)dx, \quad (13)$$

and

$$f^{(0)}[\varepsilon(x)] = \sum_{m=0}^{\infty} f_m^{(0)} \cos(mx),$$

$$f_m^{(0)} = \frac{2}{\pi(1+\delta_{m,0})}\int_0^{\pi} f^{(0)}[\varepsilon(x)]\cos(mx)dx. \quad (14)$$

Inserting Eqs.12-14 in Eq.10, we find

$$\hat{\mathcal{F}}^-(s) = -C\hat{B}(s)^{-1}\hat{f}^{(0)}, \quad (15)$$

where

$$\hat{\mathcal{F}}^-(s) = \text{col}(\mathcal{F}_1^-(s), \mathcal{F}_2^-(s), \mathcal{F}_3^-(s), \ldots), \qquad \hat{f}^{(0)} = \text{col}(f_1^{(0)}, 2f_2^{(0)}, 3f_3^{(0)}, \ldots)$$

are column vectors and B(s) is a symmetric square matrix given by

$$\hat{B}(s)_{n,m} = (n^2 + A_0)\delta_{n,m} + \frac{1}{2}[-A_{n+m} + A_{|n-m|}(1-\delta_{n,m})],$$

$$m,n = 1,2,3, \ldots . \tag{16}$$

If $\nu_{el}(k) = \nu_{el}$ is independent of k, Eq.16 reduces simply to $B(s)_{\{n,m\}}=(n^2 + A_0)\delta_{n,m}$, yielding

$$\mathcal{F}_n^-(s) = -C\frac{nf_n^{(0)}}{n^2 + A_0}, \quad A_0 = (\nu_{\text{in}} + s)(\nu_{\text{in}} + 2\nu_{\text{el}} + s)/\omega_E^2. \tag{17}$$

For a tight-binding band structure, we consider

$$\varepsilon(x) = -\sum_{n=0}^{\infty} t_n \cos nx. \tag{18}$$

The time-dependent current is given by

$$J(t) = -\frac{e}{\pi}\int_{-\pi}^{\pi} \partial\varepsilon(x)/(\hbar\,\partial x) f(k,t)dx$$

$$= -\frac{e}{\hbar\pi}\sum_{n=1}^{\infty} nt_n \int_{-\pi}^{\pi} \sin nx f(k,t)dx.$$

Changing the sign $x \rightarrow -x$ for the interval $(-\pi,0)$ and using Eq.3, we find

$$J(t) = -\frac{e}{\hbar}\sum_{n=1}^{\infty} nt_n F_n^-(t), \quad F_n^-(t) = \frac{2}{\pi}\int_0^{\pi} \sin nx F^-(x,t)dx. \tag{19}$$

For later numerical applications, we will adopt a single mode approximation and consider only the fundamental mode n=1 for simplicity:

$$\varepsilon(x) = \frac{\Delta}{2}(1 - \cos x), \tag{20}$$

where $t_0 = -t_1 = -\Delta/2$ in Eq.18. The Laplace transform of J(t) is given by

$$\mathcal{J}(s) = -\frac{e}{\hbar}\sum_{n=1}^{\infty} nt_n \mathcal{F}_n^-(s). \qquad (21)$$

The steady-state current equals

$$J(t=\infty) = \lim_{s\to 0} s\mathcal{J}(s) = -\frac{e}{\hbar}\sum_n nt_n \lim_{s\to 0} s\mathcal{F}_n^-(s), \qquad (22)$$

which can be found from Eq.15:

$$\lim_{s\to 0} s\hat{\mathcal{F}}^-(s) = -\frac{\nu_{\text{in}}}{\omega_E}\hat{B}(0)^{-1}\hat{f}^{(0)}. \qquad (23)$$

For the simple case where $\nu_{el}(k) = \nu_{el}$ is independent of k, Eq.22 reduces in view of Eq.17 to

$$J(t=\infty) = \frac{e}{\hbar}\sum_{n=1}^{\infty} n^2 t_n \frac{\nu_{\text{in}}\omega_E f_n^{(0)}}{n^2\omega_E^2 + \nu_{\text{in}}\nu_{\text{tr}}}, \qquad (24)$$

where $\nu_{tr} = \nu_{in} + 2\,\nu_{el}$ is the total transport relaxation rate.

Time-dependent current

In this section, we study the time-dependent current for the special case where the scattering rates are independent of k. In this case, we find from Eqs.17 and 21,

$$\mathcal{J}(s) = \frac{e}{\hbar}\left(1 + \frac{\nu_{\text{in}}}{s}\right)\sum_{n=1}^{\infty} \frac{n^2 t_n \omega_E f_n^{(0)}}{n^2\omega_E^2 - \nu_{\text{el}}^2 + (s+\nu_t)^2}, \qquad (25)$$

where $\nu_t = \nu_{in} + \nu_{el}$ is the total scattering rate. We find a damped non-oscillatory current for the low-field regime $\nu^2_{nE<}$ 0 and damped oscillatory solution for the high-field regime $\nu^2_{nE>} > 0$ defined by

$$\nu_{nE<} = \sqrt{\nu_{\text{el}}^2 - n^2\omega_E^2}, \quad n\omega_E \le \nu_{\text{el}},$$
$$\nu_{nE>} = \sqrt{n^2\omega_E^2 - \nu_{\text{el}}^2}, \quad n\omega_E > \nu_{\text{el}}. \qquad (26)$$

The inverse Laplace transform of Eq.25 yields

$$J(t) = \frac{e\omega_E}{\hbar}\sum_{n=1}^{\infty} n^2 t_n f_n^{(0)} \times\left[\frac{\nu_{\rm in}}{n^2\omega_E^2+\nu_{\rm in}\nu_{\rm tr}} + \exp(-\nu_t t)\left(\frac{\sinh(\nu_{nE<}t)}{\nu_{nE<}} - \frac{\nu_{\rm in}}{\nu_{nE<}}\frac{\nu_t \sinh(\nu_{nE<}t)+\nu_{nE<}\cosh(\nu_{nE<}t)}{n^2\omega_E^2+\nu_{\rm in}\nu_{\rm tr}}\right)\right], \quad n\omega_E \le \nu_{\rm el}. \tag{27}$$

By replacing $\nu_{nE<} \rightarrow i\,\nu_{nE>}$ in the above expression, we find

$$J(t) = \frac{e\omega_E}{\hbar}\sum_{n=1}^{\infty} n^2 t_n f_n^{(0)}\left[\frac{\nu_{\rm in}}{n^2\omega_E^2+\nu_{\rm in}\nu_{\rm tr}} + \exp(-\nu_t t) \times\left(\frac{\sin(\nu_{nE>}t)}{\nu_{nE>}} - \frac{\nu_{\rm in}}{\nu_{nE>}}\frac{\nu_t \sin(\nu_{nE>}t)+\nu_{nE>}\cos(\nu_{nE>}t)}{n^2\omega_E^2+\nu_{\rm in}\nu_{\rm tr}}\right)\right], \quad n\omega_E > \nu_{\rm el}. \tag{28}$$

The oscillatory contribution to the current in Eq.28 appears starting from high values of n for a given electric field. The steady state solution represented by the first terms in Eqs.27 and 28 is identical to the expression in Eq.24. Damped Bloch oscillations and the steady-state current were also studied by previous authors in three dimensions [35,41,43-45].

In the remaining part of this section, we study some interesting properties of the time-dependent solution and the steady-state current employing the single mode approximation n=1. It is interesting to note that oscillation of the current is possible only in the high-field limit $\omega_E > \nu_{el}$ when the Bloch frequency exceeds the elastic scattering rate: The condition for the onset of the oscillation depends only on the elastic scattering rate which tries to prevent the electrons from completing the cyclic motion in the Brillouin zone by reversing the direction of the motion. Visible oscillations of the current can be seen only at high fields when the oscillation rate $\nu_{1E>}$ is much larger than the damping rate ν_t. In the limit $E \rightarrow 0$, the current reduces to the linear response result $J \propto \tau_{tr}$. For high fields $\omega_E >> (\nu_{in}\,\nu_{tr})^{1/2}$, Eq.24 reduces to

$$J(t=\infty)=\frac{e\nu_{\rm in}\Delta}{2\hbar\omega_E}f_1^{(0)}. \qquad (29)$$

Namely, the steady-state current becomes linear in ν_{in} and is independent of the elastic scattering rate. It can be shown in general that the high-field current is linear in the strength of the inelastic scattering rate, independent of elastic scattering, and inversely proportional to the field beyond the relaxation-time approximation. The proof follows directly from Eq.1 as well from a microscopic expression for the electron-phonon scattering rate for the first term therein. In the high-field limit and for the steady state at t= , we note that the gradient of the distribution function $\partial f(k,t)/\partial k$ in Eq.1 is very small, yielding a nearly uniform distribution f(k,t) = f + O $(1/\omega_E)$, where f = f_0^0 is a constant defined in Eq.14. Equation 1 can then be approximated to the first order in $1/\omega_E$ as

$$\frac{\partial f(k,t)}{\partial x}\simeq-\frac{\nu_{\rm in}}{\omega_E}[f^{(0)}(\varepsilon_k)-f_0^{(0)}],$$

yielding Eq.29 via Eqs.14 and 19. The basic argument for the absence of the effect of elastic scattering for the high-field current in general relies on the fact that the initial equilibrium function f_k^0 as well as the steady-state distribution function ≈ f cancels out from the elastic scattering term of the Boltzmann equation due to energy conservation.

The steady-state current in Eq.24 becomes maximum at

$$\omega_E=\sqrt{\nu_{\rm in}/\tau_{\rm tr}} \qquad (30)$$

and equals

$$J_{\max}=\frac{e\Delta}{4\hbar}f_1^{(0)}\sqrt{\nu_{\rm in}\tau_{\rm tr}}. \qquad (31)$$

The optimum current condition in Eq.30 requires that the Bloch frequency equals $1/2\pi$ times the geometric average of the inelastic scattering rate and the transport relaxation rate. The maximum current becomes independent of the inelastic scattering rate for $\nu_{in} >> \nu_{el}$ but decreases as $(\nu_{in}/\nu_{el})^{1/2}$ in the opposite limit. Equations 30 and 31 satisfy correct scaling properties of Eq.1: Multiplying the inelastic and elastic scattering rates in Eq.1 by a constant has the effect of multiplying the field on the left hand side therein and that of Eq.30 by the same constant, while there is no other effect for the steady-state current as in Eq.31. A recent full numerical study which treats the first (inelastic scattering) term of Eq.1 microscopically in terms of electron-phonon scattering yields results numerically similar to those given by Eqs.24, 29, 30, and 31 in their scale dependences on the inelastic and elastic scattering rates and ω_E [53].

Time dependent distribution function

The time-dependent distribution function is given by

$$f(k,t) = \sum_{n=0}^{\infty} [F_n^-(t)\sin(nx) + F_n^+(t)\cos(nx)], \qquad (32)$$

where $F_n^-(t)$ was defined earlier and $F_n^+(t)$ is the expansion coefficients for

$$F^+(x,t) = \sum_{n=0}^{\infty} F_n^+(t)\cos(nx),$$

$$F_n^+(t) = \frac{2}{\pi(1+\delta_{n,0})}\int_0^{\pi} F^+(x,t)\cos(nx)dx. \qquad (33)$$

From Eqs.7,8,17, and 33, we find

$$\mathcal{F}_n^+(s) = -\frac{1}{s}\frac{n^2\omega_E^2 f_n^{(0)}}{n^2\omega_E^2 + (\nu_{\text{in}}+s)(\nu_{\text{in}}+2\nu_{\text{el}}+s)} + \frac{1}{s}f_n^{(0)}, \quad (34)$$

and

$$\mathcal{F}_n^-(s) = -\left(1+\frac{\nu_{\text{in}}}{s}\right)\frac{n\omega_E f_n^{(0)}}{n^2\omega_E^2 + (\nu_{\text{in}}+s)(\nu_{\text{in}}+2\nu_{\text{el}}+s)}. \qquad (35)$$

The inverse Laplace transform of Eqs.34 and 35 proceeds as before, yielding for the low-field case,

$$F_n^+(t) = -\frac{n^2\omega_E^2 f_n^{(0)}}{n^2\omega_E^2 + \nu_{\text{in}}\nu_{\text{tr}}}\left(1 - \exp(-\nu_t t)\frac{1}{\nu_{nE<}}[\nu_t \sinh(\nu_{nE<}t) + \nu_{nE<}\cosh(\nu_{nE<}t)]\right) + f_n^{(0)},$$

$$n\omega_E \le \nu_{\text{el}}, \qquad (36)$$

and for the high-field case,

$$F_n^+(t) = -\frac{n^2\omega_E^2 f_n^{(0)}}{n^2\omega_E^2 + \nu_{\rm in}\nu_{\rm tr}}\Bigg(1 - \exp(-\nu_t t)\frac{1}{\nu_{nE>}}[\nu_t \sin(\nu_{nE>}t) + \nu_{nE>}\cos(\nu_{nE>}t)]\Bigg) + f_n^{(0)},$$

$$n\omega_E > \nu_{\rm el}. \tag{37}$$

We also find for the low-field case

$$F_n^-(t) = -n\omega_E f_n^{(0)}\Bigg[\frac{\nu_{\rm in}}{n^2\omega_E^2 + \nu_{\rm in}\nu_{\rm tr}} + \exp(-\nu_t t)\Bigg(\frac{\sinh(\nu_{nE<}t)}{\nu_{nE<}} - \frac{\nu_{\rm in}}{\nu_{nE<}}\frac{\nu_t \sinh(\nu_{nE<}t) + \nu_{nE<}\cosh(\nu_{nE<}t)}{n^2\omega_E^2 + \nu_{\rm in}\nu_{\rm tr}}\Bigg)\Bigg],$$

$$n\omega_E \leq \nu_{\rm el} \tag{38}$$

and for the high-field case

$$F_n^-(t) = -n\omega_E f_n^{(0)}\Bigg[\frac{\nu_{\rm in}}{\nu_t^2 + n^2\omega_E^2 - \nu_{\rm el}^2} + \exp(-\nu_t t)\Bigg(\frac{\sin(\nu_{nE>}t)}{\nu_{nE>}} - \frac{\nu_{\rm in}}{\nu_{nE>}}\frac{\nu_t \sin(\nu_{nE>}t) + \nu_{nE>}\cos(\nu_{nE>}t)}{n^2\omega_E^2 + \nu_{\rm in}\nu_{\rm tr}}\Bigg)\Bigg],$$

$$n\omega_E > \nu_{\rm el}. \tag{39}$$

Note that the last term $\propto f_n^0$ in Eqs.36 and 37inserted Eq.32 yields the equilibrium Fermi function $f^{(0)}(\varepsilon_k)$.

The quantity f_n^0 can be evaluated for a general monotonous band at low temperatures $T<<\varepsilon_b$, where ε_b is the bandwidth, yielding

$$f_n^{(0)} = \frac{2a_n \sin(nx_\mu)}{n(1+\delta_{n,0})\sinh(\pi a_n)}, \tag{40}$$

where $a_n = nk_BT/\varepsilon'(x_\mu)$, $\varepsilon'(x)=d\varepsilon(x)/dx$, $\varepsilon(x_\mu)$ μ, and μ is the chemical potential. The current model yields $\varepsilon'(x_\mu) = \Delta \sin(x_\mu)/2$.

Numerical studies and discussions

For numerical studies, we consider only the fundamental mode n=1 for simplicity and assume a=100 nm. We first present numerical results for the case where ν_{el} is a constant. The time-dependent current given in Eqs.27 and 28 is displayed in Fig.10 for ν_{in} = 5x 10^{10} sec^{-1} for several values of (ν_{el}, E) where ν_{el} is in units of 10^{10} sec^{-1} and the electric field is in V/cm. A large total scattering rate ν_t damps the current oscillation quickly. Therefore, pronounced oscillations are seen only for small ν_{el} and large E, for example, for (ν_{el}, E)=(1, 20) (solid curve). The role of the lattice period in our model is to set the scale of E through the quantity Ea, which satisfies Ea<< Δ. For the upper two dash-dotted and dash-double-dotted curves, the oscillation is not visible because the oscillation frequency $\nu_{1E>}$ (defined in Eq.26) is too small. The asymptotic currents for the lower three curves corresponding to the high filed E=20 V/cm are similar in magnitude and become nearly independent of ν_{el}, while this is not true for the two upper curves corresponding to the low field E=5 V/cm. The temperature dependence is contained in the Fermi factor $f_1^{(0)}$ and also implicitly in ν_{in}.

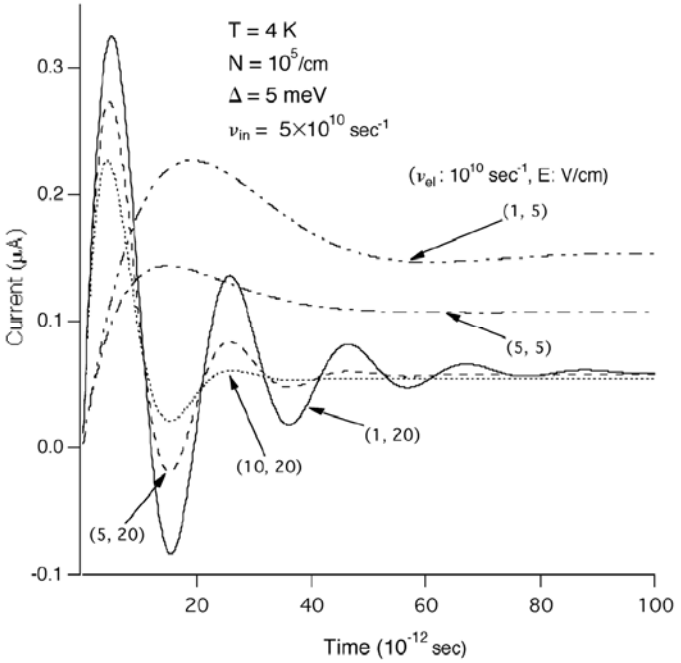

Fig. 10 The current as a function of the time for the inelastic scattering rate ν_{in}= 5x10^{10} sec^{-1} and the band width Δ=5 meV for several values of (ν_{el}, E) where ν_{el} is the elastic scattering rate in 10^{10} sec^{-1}, and E is the electric field in V/cm.

The properties of the steady-state current J( ) in Fig. 10 is studied in more detail in Fig. 11 which shows the current as a function of the field for several values of (ν_{in}, ν_{el}) given in units of 10^{10} sec^{-1}. As seen from Fig.11 and Eq.24, J( ) decays as $\propto \nu_{in}/E$ at high fields and becomes independent of ν_{in} and linear in ν_{in}. The peak of the current becomes sharper for smaller ν_{in} ¥ν_{tr}. Its magnitude depends only on the ratio ν_{in}/ν_{tr} as predicted by Eq.31 resulting in the same peak heights for the thin dash-double-dotted curve for (ν_{in}, ν_{el}) = (1,1), the thin solid curve for (5, 5), and the thick solid curve for (10, 10). The position of the peaks shifts as $E \propto (\nu_{in}/\nu_{tr})^{1/2}$. The solid curve in the

upper right inset of Fig.11 displays the temperature dependence of the prefactor $f_1^{(0)}$ for the current on the left axis. At high fields, the IV curves decay as $\propto \nu_{in} f_1^{(0)}/E$ as mentioned above, where ν_{in} is proportional to a factor $= 1 + n_{ph}$. Here, n_{ph} is the phonon occupation number for the phonon of energy $k_B T_{ph}$ and is large, viz. $n_{ph} >> 1$ at high temperatures $T >> T_{ph}$. The phonon wave number along the wire for inelastic scattering can be at most $q_{||}=2\pi/a$ and is small. The characteristic phonon energy is then of the order $c_s q_{ph} \quad k_B T_{ph}$, where $q_{ph}= (q_{||}^2+q_{perp}^2\}^{1/2}$. Here, $q_{perp} \sim 1/l$ is the transverse component of the phonon wave vector and l is the radius of the wire. The quantity T_{ph} is estimated to be 3.1 K for l = 20 nm and $c_s \approx 5x10^5$ cm/sec. The current then depends on the temperature through the factor $Z(T)= \quad f_1^{(0)}$ which is plotted on the right axis of the inset, showing a slow temperature dependence except at low temperatures, similar to the results obtained by previous authors for three dimensions [43,45].

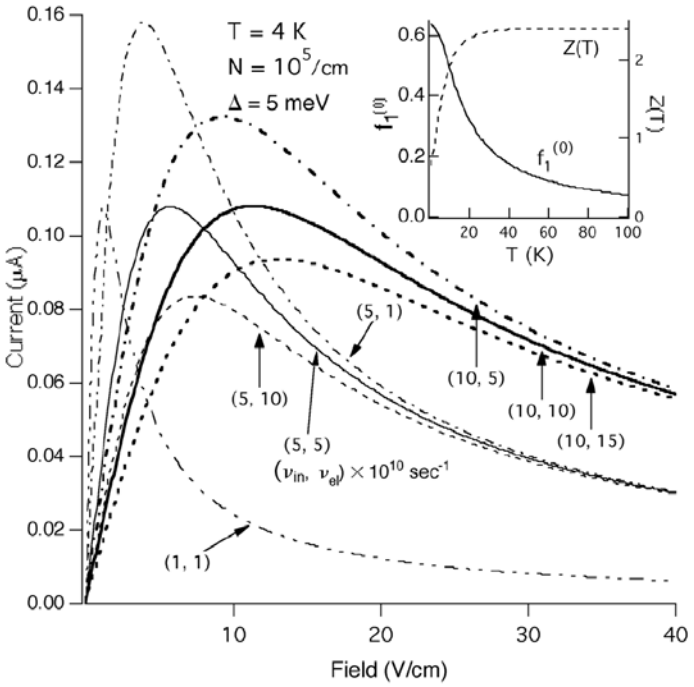

Fig. 11 The steady-state current as a function of the field for several values of energy-independent scattering rates (ν_{in}, ν_{el}) in units of 10^{10} sec^{-1} and the bandwidth Δ = 5 meV. The upper right inset shows the temperature dependences of $f_1^{(0)} (left axis) and the current J ∝ Z(T) (right axis) at high fields in the negative-differential-conductance region. The quantity Z(T) is defined in the text.

For energy-dependent $\nu_{el}(k)$, only the steady-state current can be evaluated readily in our model. Here, we consider the case where the scattering matrix element U(q) is independent of the momentum transfer q relevant for a short-ranged scattering potential, yielding

$$\nu_{\mathrm{el}}(k) = \frac{\nu_{\mathrm{el}}^*}{\pi} \int_0^{\pi} \frac{\delta dx'}{(\cos x - \cos x')^2 + \delta^2}, \qquad (41)$$

where $\delta = 2\Gamma/\Delta << 1$, G is the level damping introduced to avoid the one-dimensional van Hove singularity, and ν_{el}^{*} is the elastic scattering rate at the center of the band (i. e., x = ka = $\pi/2$). The Fourier coefficients are then given by

$$\nu_{\mathrm{el},n} \equiv \int_0^{\pi} \nu_{\mathrm{el}}(k)\cos(nx)dx$$

$$= \pi\nu_{\mathrm{el}}^{*}(-1)^{n/2}\int_0^{\infty} J_0(t)J_n(t)\exp(-\delta t)dt,$$

$$n = \text{even}, \qquad (42)$$

where Jn(t) is the nth order Bessel function, and $\nu_{el,0}$ =0 for odd integers. We calculate J( ) from Eqs.22,23,15,11, and13. The result is displayed in Fig.12 for δ = 0.01 for the same set of values of (ν_{in}, ν^{*}_{el}) as those of (ν_{in}, ν_{el}) studied in Fig.11. The results are very similar not only in the shapes and magnitudes of the curves (considering the fact that ν^{*}_{el} is somewhat different from ν_{el}) but also on the dependence of the peak heights and the positions on ν_{in} and ν^{*}_{el}.

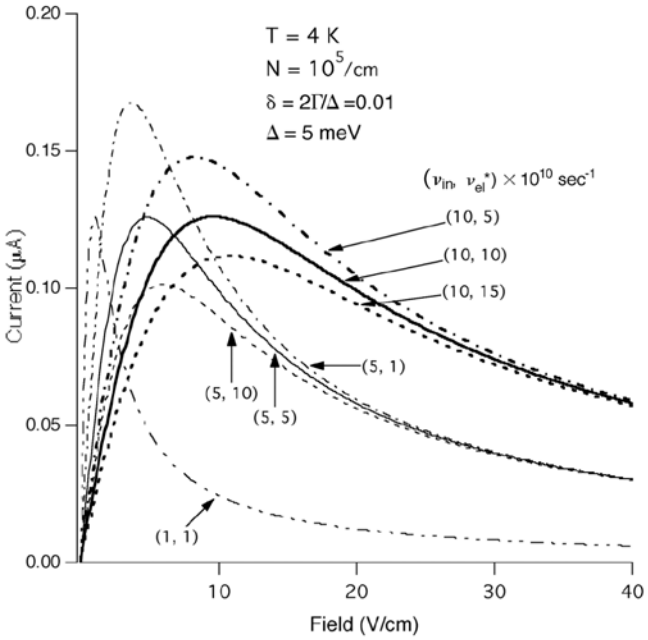

Fig. 12 The steady-state current as a function of the field for the case where the elastic scattering matrix element is independent of the momentum transfer for several values of the scattering rates (ν_{in}, ν^{*}_{el}) in units of 10^{10} sec^{-1}. Here, ν^{*}_{el} is the elastic scattering rate at the band center, Δ is the bandwidth, and Γ is the level damping introduced to avoid the one-dimensional van Hove singularity in the density of states.

Figure 12 displays the evolution of the distribution function f(k,t) in Eq.32 of an electron gas driven by an electric filed 20 V/cm for several time values corresponding to the time

points (represented by the symbols) for the current vs. time curve (solid line) of Fig. xxx repeated in the upper inset. The system starts in equilibrium (dotted curve) at t=0. The distribution function is shifted maximally to the left at t=4.7 psec (indicated by the solid circles in the figure and the inset) as shown by the thick solid curve, yielding a maximum current indicated by the solid circle in the inset. The current becomes nearly zero at t=12 psec (hollow square) and 19.5 psec (hollow triangle). However, the distribution functions (thin solid curve and dash-dotted curve) are not symmetric with respect to x=0. The dash-double-dotted curve represents the steady-state distribution function beyond t>100 psec.

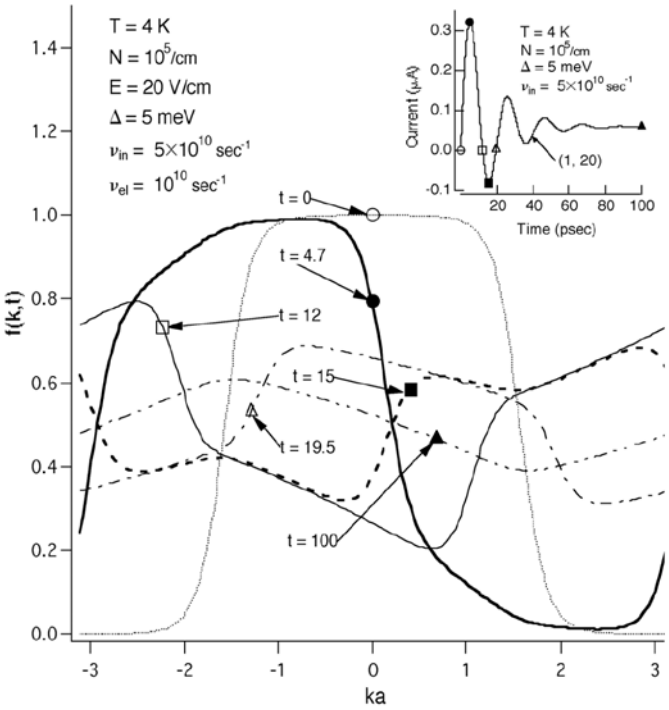

Fig. 13 The evolution of the distribution function $f(k,t)$ at several time points (represented by the symbols, each lying on the concomitant curve) in units of pico second for the electric field E=20 V/cm, the bandwidth Δ=5 meV, and the energy-independent scattering rates ν_{in} = 5x 10^{10} sec^{-1} and ν_{el} =10^{10} $sec^{-1}$$, relevant for the solid curve in Fig. 10. The symbols in the inset shows the current from Fig.10 at these time points for (ν_{el}, E) = (1, 20) where ν_{el} is in 10^{10} sec^{-1} and E is in V/cm.

Comparing the thin dotted and the thick solid curves, it is interesting to note that f(k,t) is "rigidly" shifted, roughly speaking, to the left initially, yielding the maximum current at t=4.7 psec. During this initial short time period, scattering plays a minor role compared with the acceleration and the drift imposed by a strong field. Note that the electron distribution function already spills over to the other side, i. e., ka ~ π at t=4.7, causing the current to decrease and start to oscillate. However, the maximum (minimum) value of f(k,t) decreases (increases) with time, as the electrons are scattered toward the final steady state, resulting in the flatter distribution given by the dash-double-dotted curve.

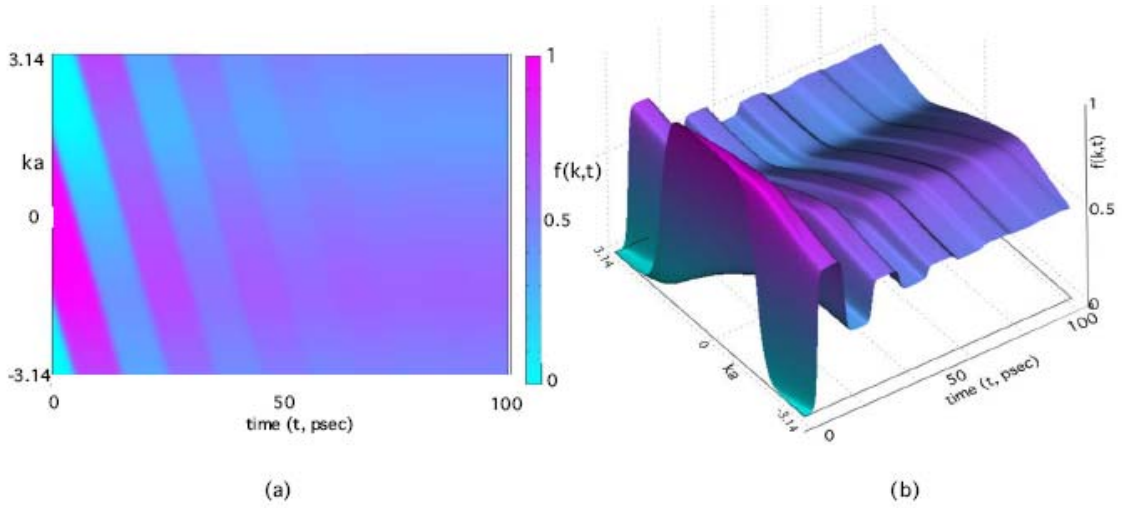

Fig. 14 (a) An image plot (i.e., the top view of (b)) and (b) a three-dimensional surface plot of the distribution function f(k,t) as a function of the time (in units of pico second) for E=20 V/cm, Δ=5 meV, N=10^5 cm^{-1}, T=4 K, and the energy-independent scattering rates ν_{in} = 5x 10^{10} sec^{-1} and ν_{el} = 10^{10} sec^{-1}, relevant for the curves in Fig.13. The function f(k,t) evolves from the Fermi function $f^{(0)}(k)$ at time t=0 when the field is applied.

The oscillations of the distribution function and the decay of the peak amplitude toward the steady state are clearly demonstrated by an image plot of f(k,t) in Fig.xxx (a) and a three-dimensional surface plot in (b). The slanted red stripes in (a) and slanted ridges in (b) at early times indicate nearly regid drift motion of the populated band of the electrons in k space from the initial Fermi distribution inside $-k_F$ k k_F toward the zone boundary at ka=-π, spilling over to the other zone boundary at ka = π with increasing time. These oscillations repeat for a longer period of time for a smaller total scattering rate ν_t according to Eq.28. Also, the oscillation frequency $\nu_{1E>} = (\omega^2_E - \nu^2_{el})^{1/2}$ becomes faster for a larger field and a smaller elastic scattering rate. The red stripes in (a) and the ridges in (b) decay eventually into a uniform steady background due to diffusive scattering with time. The horizontal dark red stripe in (a) and the redish ridge along the time axis in (b) in the region near ka ~ - 1.5 for t>40 psec represent a region with a relatively larger electron population which emerges toward the steady-state. This region of enhanced electron population is also seen near ka ~ - 1.5 from the dash-double-dotted curve in Fig.xxx.

Summary

We have presented an exact analytic result for the time-dependent current and the evolution of the distribution function in a nonlinear electric field for a degenerate and nondegenerate electron gas in a one-dimensional superlattice miniband employing a relaxation-time approximation for inelastic scattering. Our results show clearly the distinct roles played by elastic and inelastic scattering and demonstrate the dynamics of the competition between the acceleration by the electric field and scattering by phonons and static impurities in a transparent way in producing the damped Bloch oscillations and the steady-state current. They also show quantitatively how scattering damps the Bloch oscillation, the condition for the onset of the oscillations, and also the oscillation frequency. The present approach can serve as a guide to understanding the results of a

more complicated full numerical treatment. A recent full numerical study which replaces the present relaxation-time approximation of inelastic scattering by microscopic electron-phonon scattering processes yielded results very similar to those predicted here [53].

Transition from a quantum Hall ferromagnetic state to a quantum Hall spin glass state

Introduction

On the one hand, electron-electron interaction plays an important role in the two-dimensional electron system and has manifested itself in displaying many novel many body ground states. For example, due to strong Columbic interaction, at nu=1, all the electron spins align with the external magnetic field, giving rise to a ferromagnetic order [54-56]. Consequently, the energy gap (E_g) of the nu=1 state is much larger than that of bare Zeeman splitting (E_z). On the other hand, an equally important aspect in the many-body 2D electron physics is the interplay between disorder and e-e interaction. In the case of the nu=1 quantum Hall ferromagnetic state, it has been shown [57,58] that with more and more disorder, eventually, the ferromagnetic state will be destroyed and undergo a quantum phase transition to, for example, a possible quantum Hall spin glass (QHSG) state [58].

So far, previous studies on the nu=1 QH state have mainly been carried out in the clean limit, where the ground state of QHF prevails. Little, however, has been performed systematically in studying the possible phase transition from QHF to QHSG as a function of increased disorder. This difficulty mainly originates from a lack of control in realizing a tunable disorder.

In this section, we present experimental results of the nu=1 quantum Hall state in a quantum antidot array sample. In these samples, by continuously tuning the electronic potential modulation, or the "effective disorder" (ED) defined by the ratio of antidote modulation strength over the 2DES Fermi energy (E_F), we have observed a sudden collapse of its energy gap at an apparent critical disorder, indicating a possible transition from QHF to QHSG. Furthermore, in the weak disorder regime, the tilted magnetic field measurements show that the energy gap shows a concave-like B_{total} dependence, while in the strong disorder regime, the energy gap is linear with B_{total}, with slope of $3g^*\mu_B$.

Samples

The starting material is high mobility 2DES realized in a GaAs quantum well heterostructure. The well width is 300A. Before pattern, when cool in dark, the electron density is $1.6x10^{11}$ cm^{-2} and mobility is ~ $4x10^6$ cm^2/Vs. The 2DES density in the after patterned samples is tuned by the dose of a low temperature illumination using a light emitting diode, and can be tune from $0.2x10^{11}$ to $2.4x10^{11}$ cm^{-2}.

Experimental results and discussions

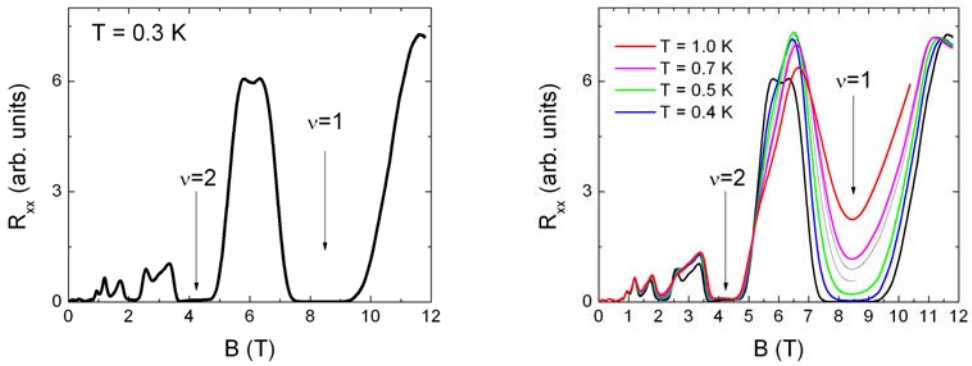

Fig.15 Quantum Hall effect in QDSL. Left panel: R_{xx} vs B at T = 0.3K. Right panel: Temperature dependence of R_{xx}.

In Figure15, we show the temperature dependence of Rxx in high magnetic fields, with nu=2 and 1 well developed at T = 0.3K. In the whole measurement temperature range, the nu=2 quantum Hall state is still strong and the resistance minimum is virtually zero. On the other hand, the nu=1 state shows a very strong temperature dependence, Rxx rising from a vanishingly small value at T = 0.3 K to Rxx ~ 100 ohm at T = 1.2K. From the activation analysis, we deduce that the energy gap at nu=1 in this sample is ~ 4K.

We have carried out a systematic density dependence of the energy gap at nu=1, as a function of 2D electron density. The electron density is continuously tuned by applying different LED illumination dose. In Figure 16, we show the energy gap as a function of the effective disorder (ED). The effective disorder is defined by $\Delta V/E_F$, where ΔV is the modulation strength, deduced from the positive MR around B=0, and E_F is the Fermi energy. It is clearly seen that at small effective disorder, the energy gap decreases rather slowly, for example, from 25 K at zero modulation for a bare sample to a 22 at ED = 0.01. The decrease accelerates as ED continues to increase, and drop sharply at ED ~ 0.08, from 22K at ED = 0.08 to ~ 2K at ED ~ 0.1.

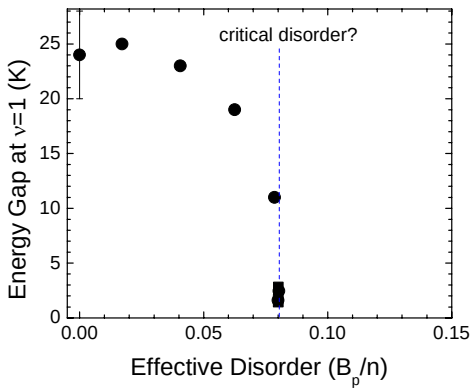

Fig.16 shows the effective disorder dependence of the nu=1 energy gap.

Figure 17 shows the angular dependence of the energy gap at nu=1 in a large modulation limit. It is clearly seen that over a large range of B field the energy gap increases roughly linearly with the total magnetic field, suggesting that in this disorder regime the Zeeman splitting is the dominant mechanism in determining the nu=1 energy gap, not the electron-electron interaction. The slope of 0.88K/T, however, is about $3g^*\mu_B$ and larger than that expected from a bare Zeeman splitting ($g^*\mu_B$).

It is surprising that the energy gap at nu=1 is significantly reduced in our QDSL sample. In comparison, the nu=1 energy gap in an unpatterned sample greatly exceeds the Zeeman energy, due to the formation of the ferromagnetic ground state. Of course, the presence of antidot makes the 2D system more disordered and will reduce the energy gap at nu=1. Our experiments show that this disorder, however, seems to affect more on the energy gap of the nu=1 state than nu=2. Indeed, in Fig.2a, the resistance minimum remains vanishingly small at 2K, while the nu=1 minimum is clearly above zero. To understand this collapse of nu=1 energy gap, we notice that in a series of paper, it was shown that the disorder plays an important role in determining the ground state at nu=1 in the quantum Hall regime, at small disorder, the ground state is a ferromagnetic state. As the disorder continues to increase, the ground state eventually becomes a quantum Hall spin glass state [58]. Our observation of the collapse of the energy gap at nu=1 at the critical effective disorder may present the first evidence of this long predicted transition.

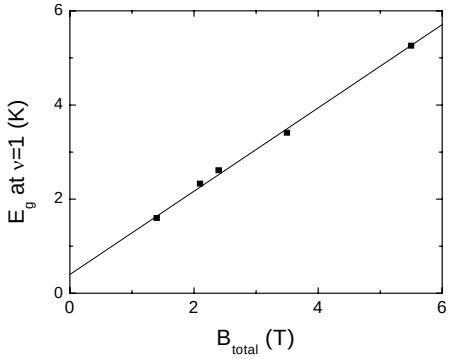

Fig.17 Energy gap at ν=1 as a function of total B field. The straight line is a linear fit.

This possible phase transition from quantum Hall ferromagnetic state to quantum Hall spin glass state is exciting. To further study this transition, we carried out a very preliminary experiment on the resistively detected NMR (RDNMR) measurements. As shown in Fig. 18, the sample was mounted on a rotating stage, and an NMR coil of 11 turns was wound around the sample. In the experiment, the filling factor was fixed and close to nu=1. All the measurements were done at the base temperature of the dilution refrigerator, ~ 20 mK. However, the electron temperature was visibly higher due to microwave radiation. In Fig. 10a, we show the ^{75}As NMR signal at the tilt angle of 11.2° and the magnetic (B) field is 7.136T. A resonance is clearly seen at 52.123 MHz. In Fig. 18b, we plot the

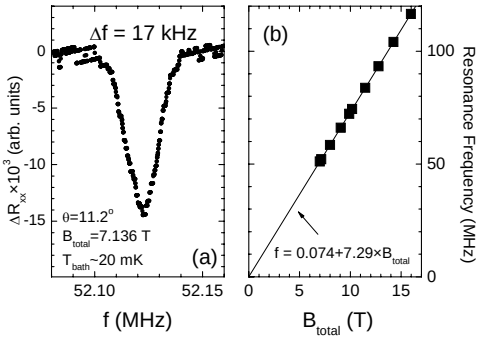

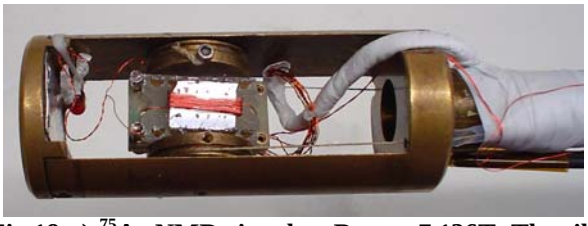

Fig.18 a) ^{75}As NMR signal at B_{total} = 7.136T. The tilt angle is 11.2°. The FWHM of the resonance at 52.123 MHz is ~ 17 KHz. b) Resonance frequency as a function of total B field. The straight line is a linear fit. The bottom picture shows the setup of NMR coil and sample on the rotating stage.

resonance frequency as a function of tilt angle or total B field (B_{total}). A linear B_{total} dependence is observed. It has a slope of 7.29 MHz/T, consistent with the gyromagnetic ratio of ^{75}As nuclei. Surprisingly, a positive finite interception of ~ 74 KHz is observed at B_{total}=0. At the present time, it is not known whether this finite value is an artifact. T_1 measurements were also performed. The above results are exiting, however, preliminary. For example, it does not tell the spin polarization directly. To gain this information, we need to perform Kight shift measurements. At the same time, we need to extend our studies to other integer quantum Hall states and the fractional quantum Hall states, and collaborate with theorists to explore in depth the underlying many-body quantum electron physics. This work will be performed in collaboration with scientists at the magnet lab in Tallahassee.

Summary

In summary, we study the energy gap at the Landau level filling nu=1 as a function of potential modulation strength in two quantum dot array sample. It is found that the energy gap of the nu=1 quantum Hall state is more or less constant as small effective disorder. As it approaches a ED of ~ 0.1, the energy gap drops quickly from ~ 22K at ED~ 0.08 to ~ 2K at ED ~ 0.10. This collapse of energy gap may present the first evidence of a proposed transition from quantum Hall ferromagnetic state to quantum Hall spin glass transition.

Some preliminary experimental results

Reversed Bloch oscillations measurements

To further study the transport properties of a Bloch oscillator, we conducted the so-called reversed Bloch oscillation measurement [15] in an anti-dot array, where the I-V characteristic was measured while the device was under an external high frequency (f = 136 GHz) radiation. In Figure 19, we show the results of dI/dV, measured in an anti-dot array sample. For sake of comparison, we also include here the dI/dV result, measured in the same sample without radiation. It is clearly seen that a resonant dip shows up at V_{DC} ~ 1.5V with radiation, while no resonant behavior is observed without radiation. It is not clear to us at the present time what is responsible for the dip at V_{DC} ~ 0.3V. Now, with a newly equipped high frequency back-wave-oscillator, more systematic measurements are now under plan.

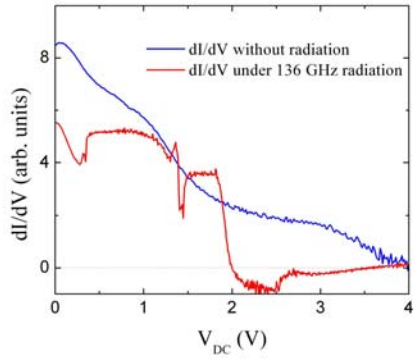

Fig.19 Reversed Bloch oscillation measurement -- dI/dV measured with and without an external high frequency radiation.

Bolometric measurements

Bolometric measurements were carried out in one QDSL device. In this type of measurement, a very sensitive thermometer, a Cernox low temperature censor from Lake Shore Cryotronics, was used and glued on the chip very close to the QDSL. The resistance of the Cernox was measured as we swept the DC bias. Strong signal was indeed observed at high DC biases. Sharp resonant-like peaks, as shown in Figure 20, were observed. At the present time, more measurements are under going to understand the possible relationship between these resonant peaks and the Bloch oscillations.

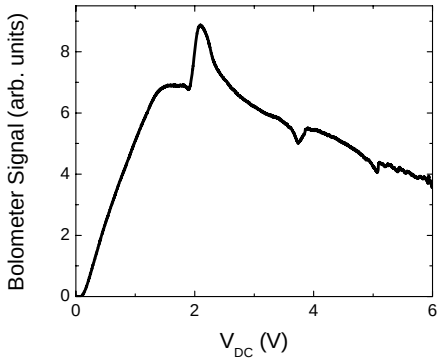

Fig.20 shows the signal of a bolometer very close to QDSL. The measurement temperature is 4K.

Time-domain THz spectroscopy measurements

The use of optical techniques to semiconductor nanostructures has generated a lot of exciting results. In the above, we have summarized our progresses on the transport studies of Bloch oscillations in QDSL. In these experiments, the observed phenomena are of the ensemble average. It is very difficult to study the coherent properties of Bloch oscillations, since the oscillatory motion of individual electron is just averaged out, and the external current flow represents the ensemble motion. To overcome this difficulty, we need to perform ultra-fast optical spectroscopy for investigating coherent Bloch oscillations in QDSL. This kind of measurements has been a powerful technique in identifying the collective excitation modes in coupled nanostructures. In collaboration with Prof. Kono's group at Rice University, we conducted time-domain THz magneto-spectroscopy measurements in QDSLs and in two-dimensional electron systems. A surprising DC electrical field induced THz phase flip was observed. Furthermore, FFT analyses of the data seem to show possible evidence of THz gain due to Bloch oscillations in QDSLs. More measurements will be carried out in this direction.

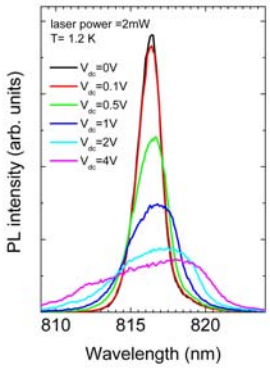

Fig. 21 Photoluminescence in QDSLs under different DC bias.

Photoluminescence in QDSLs

We also conducted the PL measurement in the 2D anti-dot arrays, under various

source-drain biases, shown in Figure 21. It was observed that the PL peak, corresponding to the GaAs band edge emission, became surprisingly broadened at high source-drain biases. It almost disappeared at V_{DC} = 4V where the system was close to the negative differential conductance regime. For the sake of comparison, we did more measurements on laser power and temperature dependence. It appears that the broadening in Figure 19 is unlikely due to an electron heating effect. More studies are needed to understand this PL result.

Reference

[1] F. Bloch, Z. Phys. **52**, 555 (1928).
[2] Condensed Matter Physics, M.P. Marder, John Wiley & Sons (2000)
[3] L. Esaki an R. Tsu, IBM J. Res. Develop. **14**, 61 (1970).
[4] J. Feldman, K. Leo, J. Shah, D.A.B. Miller, J.E. Cunningham, T. Meier, G. von Plessen, A. Schulze, P. Thomas, and S. Schmitt-Rink, Phys. Rev. B **46**, 7252 (1992).
[5] M.C. Wanke, J.S. Scott, S.J. Allen, K.D. Maranowski, and A.C. Gossard, SPIE **3617**, 148 (1999).
[6] E.S. Daniel, B.K. Gilbert, J.S. Scott, and S.J. Allen, IEEE Transactions on Electron Devices **50**, 2434 (2003).
[7] I.A. Dmitriev and R.A. Suris, Semiconductors **36**, 1364 (2002).
[8] J.R. Wendt, J.A. Simmons, J.S. Moon, M.A. Blount, W.E. Baca, and J.L. Reno, J. of Vac. Sci. & Tech. B **16**, 3808 (1998).
[9] S. H. Zaidi and S. R. J. Brueck, SPIE 3676, 371 (1999).
[10] K.K. Choi, B.F. Levine, R.J. Malik, J. Walker, and C.G. Betha, Phys. Rev. B **35**, 4172 (1987).
[11] J. Bleuse, G. Bastard, and P. Voisin, Phys. Rev. Lett. **60**, 220 (1988).
[12] E.E. Mendez, F. Agullo-Rueda, and J.M. Hong, Phys. Rev. Lett. **60**, 2426 (1988).
[13] A. Sibille, J.F. Palmier, H. Wang, and F. Mollot, Phys. Rev. Lett. **64**, 52 (1990).
[14] F. Beltram, F. Capasso, D.L. Sivco, A.L. Hutchinson, S.N.G. Chu, and A.Y. Cho, Phys. Rev. Lett. **64**, 3167 (1990).
[15] K. Utnterrainer, B.J. Keay, M.C. Wanke, S.J. Allen, D. Leonard, G. Medeiros-Ribeiro, U. Bhattacharya, and M.J.W. Rodwell, Phys. Rev. Lett. **76**, 2973 (1996).
[16] Y. Shimada, N. Sekine, and K. Hirakawa, Appl. Phys. Lett. **84**, 4926 (2004).
[17] T. Feil, H.-P. Tranitz, M. Reinwald, and W. Wegscheider, Appl. Phys. Lett. **87**, 212112 (2005).
[18] H. Sakaki, K. Wagatsuma, J. Hamasaki, and S. Saito, Thin Solid Films **36**, 497 (1976).
[19] G.J. Iafrate, D.K. Ferry, and R.K. Reich, Surface Science **113**, 485 (1982).
[20] R. Reich, Ph.D. Thesis, Colorado State University at Fort Collins (1982).
[21] G. Bernstein and D.K. Ferry, J. Vac. Sci. Tech. B **5**, 964 (1987).
[22] K. Ismail, W. Chu, D.A. Antoniadis, and H.I. Smith, Appl. Phys. Lett. **54**, 460 (1989).
[23] I.A. Dmitriev and R.A. Suris, Semiconductors **35**, 212 (2001).
[24] R.F. Gerhardt, Phys. Rev. B **48**, 9178 (1993).

[25] S.C. Lee and S.R.J. Brueck, J. of Vac. Sci. and Tech. B **22**, 1949 (2004).
[26] D. Weiss, M.L. Roukes, A. Menschig, P. Grambow, K. von Klitzing, and G. Weimann, Phys. Rev. Lett. **66**, 2790 (1991).
[27] P.H. Benton, E.S. Alves, P.C. Main, L. Eaves, M.W. Dellow, M. Henini, O.H. Hughes, S.P. Beaumont, and C.D.W. Wilkinson, Phys. Rev. B **42**, 9229 (1990).
[28] E. Schomburg, R. Scheuerer, S. Brandl, K.F. Renk, D.G. Pavel'ev, Yu. Koschurinov, V. Ustinov, A. Zhukov, A. Kovsh, and P.S. Kop'ev, Electronics Letters, **35**, 1491 (1999).
[29] E.R. Brown, J.R. Soderstrom, C.D. Parker, L.J. Mahoney, K.M. Molvar, and T.C. McGrill, Appl. Phys. Lett. **58**, 2291 (1991).
[30] H.C. Liu, Appl. Phys. Lett. **53**, 485 (1988).
[31] B.K. Ridley, Semicond. Sci. Technol. **3**, 542 (1988).
[32] K.J. Luo, K.-J. Friedland, H.T. Grahn, and K.H. Ploog, Phys. Rev. B **61**, 4477 (2000).
[33] Due to the load resistance R_0, the NDC region is pushed to higher V_{dc}, compared to Fig. 6b.
[34] S.J. Allen, Jr., H.L. Störmer, and J.C. M. Hwang, Phys. Rev. B 28, 4875 (1983)
[35] S. A. Ktitorov, G. S. Simin, and V. Ya. Sindalovskii, Sov. Phys. Solid State 13, 1872 (1972).
[36] F. G. Bass and E. A. Rubinshtein, Fiz. Tverd. Tela Lenningrad 19, 1379 (1977) [Sov. Phys. Solid Sate 19, 800 (1977)].
[37] R. A. Suris and Shchamkhalova, Fiz. Tekh. Poluprovodn. 18, 1178 (1984) [Sov. Phys. Semicond. 18, 738 (1984)].
[38] M. Artaki and K. Hess, Superlatt. Microstruct. 1, 489 (1985).
[39] H. T. Grahn, K. von Klitzing, K. Ploog, and G. H. Doehler, Phys. Rev. B 43, 12094 (1991).
[40] X. L. Lei, N. J. M. Horing, and H. L. Cui, Phys. Rev. Lett. 66, 3277 (1991).
[41] A. A. Ignatov, E. P. Dodin, and V. I. Shashkin, Mod. Phys. Lett. B 5, 1087 (1991).
[42] A. A. Ignatov, K. F. Renk, and E. P. Dodin, Phys. Rev. Lett. 70, 1996 (1993).
[43] S. Rott, P. Binder, N. Linder, and G. H. Doehler, Phys. Rev. B 59, 7334 (1999).
[44] F. Loeser, Yu. A. Kosevich, K. Koehler, and K. Leo, Phys. Rev. B 61, R13373 (2000).
[45] Yu. A. Kosevich, Phys. Rev. B 63, 205313 (2001).
[46] C. Waschke, H. G. Roskos, R. Schwedler, K. Leo, H. Kurz, and K. Koehler, Phys. Rev. Lett. 70, 3319 (1993).
[47] R. Martini, G. Klose, H. G. Roskos, H. Kurz, H. T. Grahn, and R. Hey, Phys. Rev. B 54, R14325 (1996).
[48] K. Jin, M. Odnoblyudov, Y. Shimada, K. Hirakawa, and K. A. Chao, Phys. Rev. B 68, 153315 (2003).
[49] N. Sekine and K. Hirakawa, Phys. Rev. Lett. 94, 057408 (2005).
[50] M. Foerst, G. Segschneider, T. Dekorsy, H. Kurz, and K. Koehler, Phys. Rev. B 61, R10563 (2000).
[51] V. G. Lyssenko, G. Valusis, F. Loeser, T. Hasche, K. Leo, M. M. Dignam, and K. Koehler, Phys. Rev. Lett. 79, 301 (1997)
[52] S. Rott, N. Linder, and G. H. Doehler, Phys. Rev. B 65, 195301 (2002) and references therein.
[53] D. H. Huang, private communication.

[54] S.L. Sondhi, A. Karlhede, S.A. Kivelson, and E.H. Rezayi, Phys. Rev. B **47**, 16 419 (1993).
[55] R. Tycko, S.E. Barrett, G. Dabbagh, L.N. Pfeiffer, and K.W. West, Science **268**, 1460 (1995).
[56] S.E. Barrett, G. Dabbagh, L.N.Pfeiffer, K.W. West, and R. Tycko, Phys. Rev. Lett. **74**, 5112 (1995).
[57] J. Sinova, A.H. MacDonald, and S.M. Girvin, Phys. Rev. B **62**, 13579 (2000).
[58] D.K.K. Lee, S. Rapsch, and J.T. Chalker, Phys. Rev. B **67**, 195322 (2003).

Appendix I: List of refereed publications and presentations

Publications

1. *Negative Differential Conductance in Two-Dimensional Electron Grids,* Applied Physics Letters 92, 052104 (2008).

2. *Bloch oscillations and nonlinear transport in a one-dimensional semiconductor superlattice,* Phys. Rev. B 77, 195306 (2008).

3. *Damped Bloch oscillations and dynamical localization of electron gases in quantum dot superlattices,* submitted to Phys. Rev. B.

4. *Optical probing of current-driven non-linear electrons in a quantum dot superlattice,* submitted to Phys. Rev. B.

Conference/Seminar Presentations

1. **Invited** seminar at Physics Department, California State University, Oct. 10, 2005, Los Angeles, CA.

2. **Invited** seminar at Physics Department, Indiana University, Oct. 28, 2005, Bloomington, IN.

3. **Invited** seminar at Physics Department, University of Chicago, Oct. 31, 2005, Chicago, IL.

4. **Invited** seminar at Physics Department, University of Virginia, Nov. 10, 2005, Charlottesville, VA.

5. **Invited** talk at the National Nanotechnology Infrastructure Network annual review meeting, Feb. 26-28, 2006, Austin, TX.

6. **Invited** seminar at the National High Magnetic Field Laboratory, April 12, 2006, Tallahassee, FL

7. **Invited** to present a paper at the International Conference on Strongly Correlated Low-Dimensional Systems, July 2-8, 2006, Ascona, Switzerland. (declined)

8. **Invited** talk at the International Workshop on “Interactions, Excitations, and

Broken Symmetries in Quantum Hall Systems", Oct. 2-7, 2006, Dresden, Germany.

9. **Invited** talk at the International Workshop on "Emergent Phenomena in Quantum Hall system-2", Penn State University, June 13-17, 2007.

10. **Invited** seminar at Universidad Autonoma Metropolitana Azcapotzalco, July 17, 2008, Mexico City, Mexico.

11. One contributed talk at the American Physical Society 2006 March Meeting, March 13-17, 2006, Baltimore, MD.

12. Two contributed talks at the American Physical Society 2007 March Meeting, March 5-9, 2007, Denver, CO.

13. One contributed talk at the American Physical Society 2008 March Meeting, March 10-14, 2008, New Orleans, LA.

14. One oral talk at the International Conference on Superlattice, Nanostructure and Nanodevices (ICSNN 2008), August 3-8, 2008, Natal, Brazil. (cancelled)

Distribution

1 MS 0123 LDRD Office, 01011

1 MS 1086 Wei Pan, 01123
1 MS 1415 Ken Lyo, 01123
1 MS 1303 John Reno, 01132
1 MS 1082 Joel Wendt, 01725
1 MS 1086 Dan Barton, 01123
1 MS 1082 Mike Wanke, 01725
1 MS 1082 John Seamons, 01725
1 MS 1056 Edward Bielejec, 01111
1 MS 1303 Michael Lilly, 01132
1 MS 1303 Mark Lee, 01132
1 MS 1421 Jerry Simmons, 01120
1 MS 1427 Julia Phillips, 01100

1 MS 0899 Technical Library, 9536 (electronic copy)


Sandia National Laboratories